Journal of The Electrochemical Society

OPEN ACCESS

Towards Optimised Cell Design of Thin Film Silicon-Based Solid-State Batteries via Modelling and Experimental Characterisation

To cite this article: Pooja Vadhva *et al* 2022 *J. Electrochem. Soc.* **169** 100525

Journal of The Electrochemical Society, 2022 **169** 100525

Towards Optimised Cell Design of Thin Film Silicon-Based Solid-State Batteries via Modelling and Experimental Characterisation

Pooja Vadhva,[1] Adam M. Boyce,[1,2] Alastair Hales,[3] Mei-Chin Pang,[3,4] Anisha N. Patel,[3] Paul R. Shearing,[1,2] Gregory Offer,[2] and Alexander J. E. Rettie[1,z]

[1]*Electrochemical Innovation Lab, Department of Chemical Engineering, University College London, London WC1E 7JE, United Kingdom*
[2]*The Faraday Institution, Quad One Becquerel Avenue Harwell, Didcot OX11 0RA, United Kingdom*
[3]*Department of Mechanical Engineering, Imperial College London, London SW7 1AY, United Kingdom*
[4]*BASF SE, Carl-Bosch-Strasse 38, 67056 Ludwigshafen am Rhein, Germany*

To realise the promise of solid-state batteries, negative electrode materials exhibiting large volumetric expansions, such as Li and Si, must be used. These volume changes can cause significant mechanical stresses and strains that affect cell performance and durability, however their role and nature in SSBs are poorly understood. Here, a 2D electro-chemo-mechanical model is constructed and experimentally validated using steady-state, transient and pulsed electrochemical methods. The model geometry is taken as a representative cross-section of a non-porous, thin-film solid-state battery with an amorphous Si (*a*-Si) negative electrode, lithium phosphorous oxynitride (LiPON) solid electrolyte and $LiCoO_2$ (LCO) positive electrode. A viscoplastic model is used to predict the build-up of strains and plastic deformation of *a*-Si as a result of (de)lithiation during cycling. A suite of electrochemical tests, including electrochemical impedance spectroscopy, the galvanostatic intermittent titration technique and hybrid pulse power characterisation are carried out to establish key parameters for model validation. The validated model is used to explore the peak interfacial (*a*-Si|LiPON) stress and strain as a function of the relative electrode thickness (up to a factor of 4), revealing a peak volumetric expansion from 69% to 104% during cycling at 1C. The validation of this electro-chemo-mechanical model under load and pulsed operating conditions will aid in the cell design and optimisation of solid-state battery technologies.
 [DOI: 10.1149/1945-7111/ac9552]

Manuscript submitted June 20, 2022; revised manuscript received September 3, 2022. Published October 19, 2022.

Supplementary material for this article is available online

The global micro-battery market size is currently estimated to be US $326 million and projected to increase to US $842 million by 2026[1,2]; driven primarily by the proliferation of wearable, portable electronic and Internet of Things devices. The safety and reliability of these cells are of paramount importance, in addition to them being lightweight and exhibiting high power and energy densities.[2] Lithium-ion batteries (LIBs) are approaching practical limits in terms of safety and energy density due to the flammable liquid electrolytes used. Alternative cell designs such as solid-state batteries (SSBs) promise improvements in these aspects by replacing the liquid electrolyte with a solid electrolyte (SE) and using Li metal as the negative electrode ($\approx 10\times$ greater specific energy density than graphite used in LIBs) respectively. However, the use of metallic Li presents challenges due to high reactivity and inhomogeneous plating and stripping processes which can lead to dendrite formation and cell failure.

Silicon negative electrodes also feature a high specific capacity (>3500 mAh g^{-1}) and a low electrochemical potential (0.3 V vs Li/Li^+),[3] but do not suffer from dendrite formation. Furthermore, Si is abundant and does not require strict air and moisture-free processing, therefore it has the potential to be a cost-effective alternative to Li metal as a negative electrode material in next generation batteries. On the other hand, Si exhibits a large volumetric expansion during lithiation (as much as 300%) causing severe mechanical degradation and continuous interphase formation in cells using liquid electrolytes. Moving to a solid-state system may have advantages in this respect: stable interphase formation has been achieved using sulfide-based SEs,[4] enabling stable full cell cycling over 500 cycles[5] and in half-cell experiments, Ping et al.[6] used an oxide-based SE to limit Si expansion compared to a liquid electrolyte, attributing this effect to the mechanical rigidity of the SE. However, many fundamental aspects of Si-based SSBs are poorly understood, such as the solid-solid coupling between Si and the SE during this large volumetric expansion,[7–10] and there are limited studies of Si-based SSBs that are paired with conventional positive electrode materials.[5–7,11–13] Furthermore, while models of Si-based LIBs are well described in the literature,[14–18] those of SSBs with Si negative electrodes are lacking, especially those validated against experimental data for cycling and pulsing conditions. By improving our understanding of the stress-strain relationship at the *a*-Si|SE interface, the mechanical properties of the SE and cell dimensions may be tailored to limit Si expansion, thereby increasing cell lifetime and enabling high power micro-batteries with potential implications for large-format solid-state cells.

In this study, a 2D electro-chemo-mechanical model was built and validated using a suite of experimental electrochemical tests on a thin-film amorphous silicon (*a*-Si)|LiPON|$LiCoO_2$ SSB. First, the model formation is described, whilst the numerical methods section discusses the material parameters and simulation details. Next, the experimental methods sections presents the electrochemical behavior during initial cell formation, steady state conditions and pulsed conditions using the galvanostatic intermittent titration technique (GITT) and hybrid pulse power characterisation (HPPC). In several cases, these results were used to parameterise the model. Subsequently, model agreement with charge/discharge curves acquired at 1C rate was investigated followed by further validation against the HPPC response. Finally, we present the effects of varying relative electrode thickness (up to a factor of 4) on the mechanical stresses and strains experienced in the SSB model.

Model Formulation

A schematic of the SSB is illustrated in Fig. 1: we define the current collectors (CCs), SE separator, *a*-Si negative and LCO positive electrodes, where t_{cc}, t_{sep}, t_{ne}, t_{pe} are their respective thicknesses. Also, note the orthogonal coordinate system, where the *x*, *y*, and *z* coordinates are the thickness, length and width of the thin film SSB respectively. The ensuing electro-chemo-

[z]E-mail: a.rettie@ucl.ac.uk

mechanical framework assumed a 2D geometry (given the film-like nature of the SSB) with Li transport in 1D and mechanical properties with a plane strain mechanical treatment in *x*-*y* (Fig. 1). For computational efficiency, a small sub volume of the overall cell thickness *x*, was modelled, which was assumed to be representative of the cell.

Solid electrolyte.—The SE is described by concentrated solution theory[19] and with Li^+ ions assumed to be the only mobile species present. This is a reasonable assumption as the transference number has been experimentally measured to be close to unity for LiPON.[6,9] The Nernst-Plank equation is used to model ion conduction in the bulk SE region

$$J_b = -D_b \nabla c_b + \frac{z_i F}{RT} D_b c_b \nabla \varphi_b \quad [1]$$

where J_b is the flux across the bulk electrolyte, z_i is the species charge, F is Faraday's constant (96,485 C mol^{-1}), D_b is the diffusion coefficient, c_b is the concentration of the bulk SE and φ_b is the electric potential across the medium. Given that the electrolyte is a solid body, convection terms were neglected. In addition, the system must obey charge conservation

$$\nabla \cdot \boldsymbol{i_b} = 0 \quad [2]$$

where $\boldsymbol{i_b}$ is the current in the bulk SE (bold symbols represent vector quantities). The stress in the SE obeys mechanical equilibrium such that body forces are neglected

$$\nabla \cdot \boldsymbol{\sigma_b} = 0 \quad [3]$$

where σ_b is the Cauchy stress tensor. The SE is assumed to obey Hooke's Law: $\sigma_b = C_b \times \varepsilon_b$, where C_b is the stiffness matrix, and in this instance, we consider the model to be isotropic with Young's modulus, E_b and Poisson's ratio, ν_b. A small strain formulation is considered, where the total strain ε_b is obtained by solving for the displacement field, $\boldsymbol{u}$ in the SE

$$\boldsymbol{\varepsilon_b} = \frac{1}{2}((\nabla \boldsymbol{u})^T + \nabla \boldsymbol{u}) \quad [4]$$

Positive electrode.—Like the SE, the LCO positive electrode is assumed to observe mechanical equilibrium (Eq. 3), while a similar small strain formulation and isotropic Hooke's law are employed, with stress $\boldsymbol{\sigma}_p$, a total strain $\boldsymbol{\varepsilon}_p$, stiffness matrix $\boldsymbol{C}_p$, Young's modulus E_p and Poisson's ratio, ν_p. Here, there is diffusion induced strain $\boldsymbol{\varepsilon}_p^{ch}$, and consequently we must decompose the total strain $\boldsymbol{\varepsilon}_p$, into an elastic component $\boldsymbol{\varepsilon}_p^e$, and a diffusion-related component: $\boldsymbol{\varepsilon}_p = \boldsymbol{\varepsilon}_p^e + \boldsymbol{\varepsilon}_p^{ch}$, where $\boldsymbol{\varepsilon}_p^{ch}$ is given as

$$\varepsilon_p^{ch} = \frac{1}{3}\Omega_p(c_p - c_{p0})\mathbf{I} \quad [5]$$

where c_p is the Li concentration, c_{p0} is the initial Li concentration, Ω_p is the partial molar volume and $\mathbf{I}$ is the identity tensor. Solid-state diffusion in the positive electrode is modelled using Fick's first law with an additional contribution due to diffusion-induced swelling (hydrostatic) stresses

$$\boldsymbol{J_p} = -D_p \nabla c_p + \frac{\Omega_p c_p}{RT} \nabla \boldsymbol{\sigma}_{p,H} \quad [6]$$

where $\boldsymbol{\sigma}_{p,H} = \mathrm{tr}[\boldsymbol{\sigma}]/3$, D_p is the diffusion coefficient, and $\boldsymbol{J_p}$ is the flux, where the subscript p detonates these parameters to relate to the positive electrode region. Fick's second law describes the transient transport of Li in the electrode

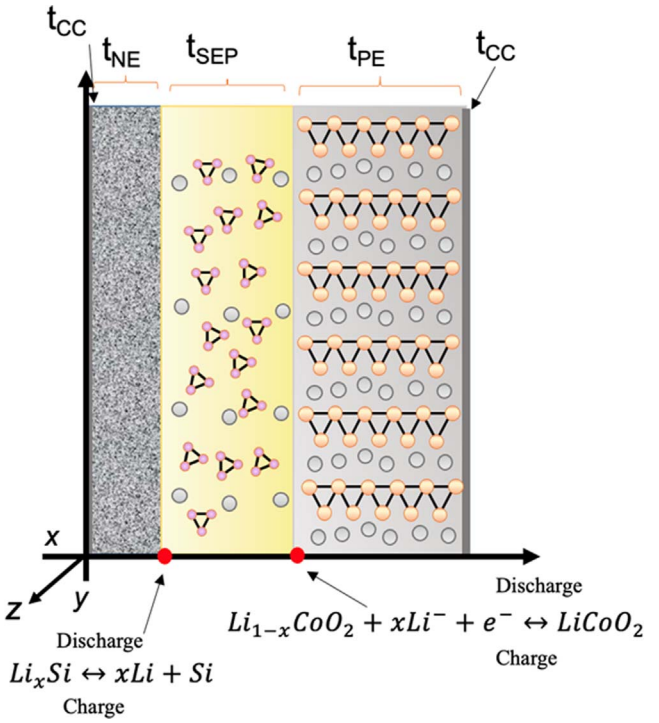

Figure 1. The 2D cross-sectional schematic of the thin film SSB used in the COMSOL model. Note that the atomic arrangements are purely for illustrative purposes and that atomistic simulations were not performed in this study.

$$\frac{\partial c_p}{\partial t} = \nabla \cdot \boldsymbol{J_p} \quad [7]$$

Current flow was modelled using Ohm's law

$$\boldsymbol{i}_p = -K_p \nabla \varphi_p \quad [8]$$

where $\boldsymbol{i}_p$ and K_p are the current and electronic conductivity across the positive electrode respectively. Finally, charge conservation was observed

$$\nabla \cdot \boldsymbol{i}_p = 0 \quad [9]$$

Negative electrode.—It is known that thin film electrodes at a given capacity do not display a difference in stress (across the thickness of the electrode) unless the electrode materials experience plastic deformation.[20] If only elastic deformation of the electrodes occurs, then hysteresis would be not observed as the loading and unloading during cycling would occur along the same stress path. It is important to highlight that other stress contributions could affect the hysteresis loop, such as the Li concentration gradients at the electrode interfaces. However, as LCO is not expected to plastically deform due to its higher Young's modulus and hardness than *a*-Si (even when fully lithiated)[21] it is reasonable to assume that voltage hysteresis (as observed experimentally in the electrochemical testing section) is primarily due to plastic deformation of *a*-Si occurring during discharge.

Upon lithiation Si can exhibit nominal strains up to 300%, thus it is appropriate to adopt a viscoplastic-type yield model.[15,20] The following approach was adapted from Di Leo et al.[16] who experimentally validated their electro-mechanical model against half-cell curvature data using mechanical measurements of an *a*-Si electrode and a liquid electrolyte.[15,16] To the best of our knowledge, analogous experiments have not been reported for *a*-Si with a solid

electrolyte. The method is summarised as follows: we consider finite deformation kinematics with large elastic-plastic strains and multiplicative decomposition of the deformation gradient, $\boldsymbol{F}=\boldsymbol{F}^{\mathrm{e}}\boldsymbol{F}^{\mathrm{p}}\boldsymbol{F}^{\mathrm{ch}}$, where the superscripts represent the elastic, volume-preserving plastic, and lithiation-induced deformation gradients. The lithiation-induced deformation gradient is given as $\boldsymbol{F}^{\mathbf{ch}}=(1+\Omega(c_n-c_{n0}))^{1/3}$, such that $\bar{c}=c_n/c_{n,max}$, where c_{n} is the Li concentration and $c_{\mathrm{n,max}}$ is the maximum Li concentration in the negative electrode. The plastic deformation evolves as

$$\dot{\boldsymbol{F}}^{\mathrm{p}}=\dot{\varepsilon}^{\mathrm{p}}_{\mathrm{eq}}\left(\frac{3\boldsymbol{\sigma}}{2\sigma_{\mathrm{eq}}}\right)\boldsymbol{F}^{\mathrm{p}} \quad [10]$$

where $\dot{\varepsilon}^{\mathrm{p}}_{\mathrm{eq}}>0$ is the equivalent plastic strain rate and $\sigma_{\mathrm{eq}}=\sqrt{3/2}\,|\boldsymbol{\sigma}|$ is the equivalent stress. During plastic flow, we take the equivalent strain rate to be

$$\dot{\boldsymbol{\varepsilon}}^{p}_{\mathrm{eq}}=\begin{cases}0 & if\ \sigma_{\mathrm{eq}}\leqslant\sigma_{\mathrm{Y}}(\bar{c})\\ \dot{\varepsilon}_0\left(\frac{\sigma_{\mathrm{eq}}-\sigma_{\mathrm{Y}}(\bar{c})}{\sigma_*}\right)^m & if\ \sigma_{eq}>\sigma_Y(\bar{c})\end{cases} \quad [11]$$

whereσ_* is a stress-based constant, $\dot{\varepsilon}_0$ is a reference plastic strain-rate and m is a strain-rate related fitting parameter. The concentration-dependent yield stress, $\boldsymbol{\sigma}_{\mathrm{Y}}(\bar{c})$ is given as

$$\sigma_{\mathrm{Y}}(\bar{c}_{\mathrm{n}})=\sigma_{\mathrm{sat}}+(\sigma_0-\sigma_{\mathrm{sat}})e^{-\frac{\bar{c}_n}{\bar{c}_*}} \quad [12]$$

where σ_0, σ_{sat}, c_* are positive-valued stress-related fitting parameters. As with the positive electrode, diffusion of Li within the negative electrode is captured using Fick's Law and an additional swelling term, analogous to Eq. 6

$$\boldsymbol{J}_{\mathbf{n}}=-D_n\nabla c_n+\frac{\Omega_{\mathrm{n}}c_{\mathrm{n}}}{RT}\nabla\sigma_{\mathrm{n,H}} \quad [13]$$

As in the studies of Sethuraman et al.[20] and Di Leo et al.,[16] we neglect quadratic, higher-order stress-related terms by assuming their negligible influence on the overall response. As before, Fick's second law provides a description of transient diffusion

$$\frac{\partial c_{\mathrm{n}}}{\partial t}=\nabla\cdot\boldsymbol{J}_{\mathbf{n}} \quad [14]$$

As before, Ohm's law describes current flow

$$\boldsymbol{i}_{\mathrm{n}}=-K_{\mathrm{n}}\nabla\varphi_{\mathrm{n}} \quad [15]$$

with $\boldsymbol{i}_{\mathrm{n}}$ and K_{n} being the current and electronic conductivity, across the negative respectively, and charge conservation is observed

$$\nabla.\,\boldsymbol{i}_{\mathrm{n}}=0 \quad [16]$$

Charge transfer kinetics.—It is necessary to impose boundary conditions at the interfaces of the SE and electrode in order to accurately solve model equations. By doing so the charge transfer reactions and the additional stress overpotential required for lithiation to proceed are captured. The charge transfer rate is commonly expressed using a Butler-Volmer type equation

$$i_{\mathrm{BV}}=i_0\left(\exp\left(\frac{\alpha_n F\eta_{\mathrm{n}}}{RT}\right)-\exp\left(-\frac{\alpha_p F\eta_{\mathrm{p}}}{RT}\right)\right) \quad [17]$$

where α_n and α_p are the negative and positive charge transfer coefficients respectively. The local exchange current density, i_0 is dependent on both Li and bulk electrolyte concentrations

$$i_0=F(k_{\mathrm{p}})^{\alpha_{\mathrm{n}}}(\mathrm{k}_n)^{\alpha_{\mathrm{p}}}(c_i-c_{i,max})^{\alpha_{\mathrm{n}}}(c_{\mathrm{i}})^{\alpha_{\mathrm{p}}}\left(\frac{c_b}{c_{b,ref}}\right)^{\alpha_{\mathrm{n}}} \quad [18]$$

where the subscript i is n or p depending on the interface, $c_{\mathrm{b,ref}}$ is a reference SE concentration, c_{max} is the maximum SE concentration and the rate constants of the positive and negative electrodes are k_{p} and k_n respectively. The total overpotential η_{i}, is expressed as

$$\eta_{\mathrm{i}}=\varphi_{\mathrm{i}}-\varphi_{\mathrm{b}}-U_{\mathrm{i}}-\frac{\Omega_{\mathrm{i}}\sigma_{\mathrm{H,i}}}{F} \quad [19]$$

where U_{i} is the open circuit voltage, and additional overpotentials due to diffusion-induced hydrostatic stress $\sigma_{\mathrm{H,i}}$ and the initial partial molar volume Ω_{i}, are incorporated via the final term on the right-hand side of Eq. 19.[22]

Boundary and initial conditions.—Consider the coordinate system (x, y, z) in Fig. 1. At the positive current collector (CC), we apply a current density $\boldsymbol{i}_{\mathrm{cc}}\cdot\boldsymbol{n}_{\mathrm{cc,p}}=i_{\mathrm{in}}$ at $x=(t_{\mathrm{cc,n}}+t_{\mathrm{ne}}+t_{\mathrm{sep}}+t_{\mathrm{pe}}+t_{\mathrm{cc,p}})$, where $\boldsymbol{n}_{\mathrm{cc,p}}$ is the unit normal vector pointing outwards from the positive CC surface in the positive z-direction. The applied current density i_{in} at 1C discharge, is calculated based on the sub volume of the cell. Since the maximum accepted quantity of Li for the given electrode material, $c_{p,max}$: the current density is given as $i_{\mathrm{in}}=c_{p,max}FV_p/t_0A$, where the area is in the dimensions of the cell in the z, y coordinates, $A=zy$ and $t_0=3600$ s. At the negative current collector, a potential of $\varphi_{\mathrm{p}}=0$ V is applied at $x=0$.

We prescribe the thin film SSB to be fixed in all directions to the positive current collector surface, i.e. $\boldsymbol{u}_{\mathrm{cc}}\cdot\boldsymbol{n}_{\mathrm{cc,p}}=0$ at $x=(t_{\mathrm{cc,n}}+t_{\mathrm{ne}}+t_{\mathrm{sep}}+t_{\mathrm{pe}}+t_{\mathrm{cc,p}})$, whilst the negative CC surface remains unconstrained. Given that a small sub volume of the electrode is modelled in the y-direction, it is appropriate to apply symmetry boundary conditions for species fluxes, displacements and potentials.

At the interface between the separator and the electrodes, we specify that the electronic current flow must be zero: $\boldsymbol{i}_{\mathrm{i}}\cdot\boldsymbol{n}_{\mathrm{sep,i}}=0$, where $\boldsymbol{n}_{\mathrm{sep}}$ is the unit normal vector to the interface between the electrode and the separator, pointing in the direction away from the electrodes. This ensures that only the ionic current is permitted across this interface. At the electrolyte-electrode interface we observe a flux of Li into the electrode, or Li^+ ions into the electrolyte as a result of the charge transfer reaction. The fluxes are as follows: $\boldsymbol{J}_{\mathrm{b}}\cdot\boldsymbol{n}_{\mathrm{sep}}=-i_{\mathrm{BV}}/F$ and $\boldsymbol{J}_{\mathrm{i}}\cdot\boldsymbol{n}_{\mathrm{i}}=-i_{\mathrm{BV}}/F$, where $\boldsymbol{n}_{\mathrm{i}}$ is the normal vector pointing from the electrolyte to the electrodes. We also prescribe a current density at this interface: $\boldsymbol{i}_{\mathrm{b}}\cdot\boldsymbol{n}_{\mathrm{sep}}=-i_{\mathrm{BV}}$ and $\boldsymbol{i}_{\mathrm{i}}\cdot\boldsymbol{n}_{\mathrm{i}}=-i_{\mathrm{BV}}$. An initial Li concentration in the electrodes, c_{i0}, is prescribed, whilst the initial concentration in the electrolyte is given by c_{b0}. The electrode and all associated constituent domains are assumed to be in an initially unstressed state.

To summarise, the strain type simulated in the SE and positive electrode domains is linear elastic whereas for the negative electrode (a-Si) elastic-viscoplastic behavior is modelled. The three types of strains occurring within the negative electrode are elastic, volume-preserving plastic, and lithiation-induced deformation gradients. The electrode and SE are not expected to plastically deform due to their greater Young's moduli and hardness at all stages of lithiation.

Numerical methods

Material parameters.—The mechanical and electrochemical parameters used in the model were either previously reported values from the literature or experimentally determined in this study (Table I). LCO and LiPON were assumed to be isotropic linear-elastic solids, whereas a-Si was treated as an isotropic elastic-viscoplastic solid with a Li concentration-dependent Young's modulus and yield strength as defined in Eq. 12. The elastic properties of a-Si vary with state of lithiation (SoL) during cell

Table I. Model parameters.

	Parameter	Units	Value	Source
Electrochemical	D_b	$m^2\ s^{-1}$	1.7×10^{-16}	Ref. 23
	c_{b0}	mol m^{-3}	1000	—
	$c_{p,max}$	mol m^{-3}	5.19×10^4	Ref. 24
	$c_{n,max}$	mol m^{-3}	1.55×10^5	Calculated
	c_{n0}	mol m^{-3}	$0.05 \times c_{Si,max}$	—
	c_{p0}	mol m^{-3}	$0.95 \times c_{LCO,max}$	—
	α_n, α_p	1	0.5	—
	K_b	S cm^{-1}	2.3×10^{-6}	Electrochemical impedance spectroscopy (EIS)
	K_n	S cm^{-1}	0.33	Ref. 25
	K_p	S cm^{-1}	1×10^{-5}	Averaged from Ref. 21
Elastic	E_p	GPa	191	Ref. 21
	E_n	GPa	$f(c_n/c_{n,max})$	Ref. 16
	E_b	GPa	77	Ref. 26
	υ_p	1	0.24	Ref. 21
	υ_b	1	0.25	Ref. 26
	υ_n	1	$f(c_n/c_{n,max})$	Ref. 16
	Ω_n	$m^3\ mol^{-1}$	8.8×10^{-6}	Ref. 27
	Ω_p	$m^3\ mol^{-1}$	-1×10^{-7}	Ref. 12
Plastic	σ_{Y0}	GPa	0.9	Ref. 17
	σ_{sat}	GPa	0.4	Ref. 17
	$\dot{\epsilon}$	1/s	2.3×10^{-3}	Ref. 17
	m	1	2.94	Ref. 17
Rate kinetics	k_n, k_p	mol $m^{-2}\ s^{-1}$	1.3×10^{-5}	Obtained from 1C cycling data
	U_p	V	$f(c_n/c_{n,max})$	Ref. 24

cycling. The Young's modulus and Poisson's ratio vary between the elastic limits of pure Li and *a*-Si depending on SoL. This produces a non-linear trend which is captured in the model (a detailed explanation of these parameters can be found in the study by Leo et al.[16]). The current collectors were assumed to be electronically conductive, linear elastic solids with Young's moduli of ≈100 GPa. Finally, the universal gas constant, R was taken as 8.314 J mol^{-1} K^{-1}, and all simulations and experiments were carried out at a temperature, T of 298 K.

Electrochemical properties often vary as a function of composition. The diffusion coefficient was experimentally estimated as a function of state of charge (SoC) for *a*-Si and LCO using the galvanostatic intermittent titration technique (GITT). Diffusion through the SE was given by D_b, reported by Raijmakers et al.[23] The initial concentration of Li^+ ions, c_{b0} was parametrised in the study to give the best fit to the experimental 1C data. The maximum concentration $c_{Si,\ max}$ of Li in Li_ySi was estimated using the equation: $c_{Si,\ max} = y\rho_{Si}$. Here y represents the Li stoichiometry in Li_ySi and ρ_{Si} is the theoretical maximum molar density of the hosting material. By analysing the quantity of Li extracted from LCO during charging, the amount of Li alloyed with the *a*-Si electrode was calculated. The upper voltage limit was 4 V and by extrapolation to the open circuit voltage (OCV) of LCO, the amount of Li extracted from LCO, y was quantified. It should be noted that the value of y must be normalised by the LCO thickness.

Simulation and validation details.—The 2D electro-chemo-mechanical model was created using the finite element modelling software package, COMSOL Multiphysics (v5.6, Sweden). The 2D geometry in this study is used to model the mechanical properties in the *x*-*y* plane. The mesh consisted of approximately 4,000 quadratic elements with 94,000 degrees of freedom, while the solutions were found to be mesh independent. The Parallel Direct Sparse Solver (PARDISO) was used to solve the discretised transport, electrode kinetics and deformation kinematics equations. A segregated approach was used, which involved solving the coupled field variables in a sequential staggered manner. Time stepping was handled using 2nd order backward Euler differentiation, whilst time step sensitivity analysis was performed.

Experimental Characterisation and Testing Procedures

Experimental set-up.—A commercial thin-film SSB was supplied by Ilika Technologies Ltd (Southampton, UK). The cell had a capacity of 250 μAh, comprising an *a*-Si negative electrode, a LiPON SE and a crystalline LCO positive electrode sputtered on top of a substrate using vacuum processing methods. The SSB cell was mounted on a printed circuit board with embedded electrical connections and housed inside a thermal chamber. A potentiostat (Biologic EC-lab) was used to execute cell cycling protocols and a thermocouple was attached to the cell to monitor its temperature which was recorded using a data logger (PicoLog TC-08).

Cell formation and steady state electrochemical tests.—The cell was formed using 5 charge/discharge cycles at C/5 and differential capacity ($\frac{dQ}{dSoC}$) analysis performed to reveal electrode processes. Since the $\frac{dQ}{dSoC}$ analysis of the full cell contains information from both electrodes, comparison with half-cell data from literature was used to assign the peak contributions from the *a*-Si and LCO.[21,28] The $\frac{dQ}{dSoC}$ data were compared during the first formation cycle and after subsequent cycling at 1C.

The open circuit voltage (OCV) as a function of SoC was determined for the full cell after relaxation for 24 h at 10% capacity increments. A pseudo-OCV was measured using a small cycling current of C/30. Electrochemical impedance spectroscopy (EIS) measurements were taken at each 10% SoC interval after 24 h relaxation during charge and discharge. During EIS, a 5 mV voltage perturbation and a frequency range of 1 mHz to 1 MHz were used. Nyquist plots (-Im(Z) vs Re(Z)) were fitted with an equivalent circuit model (ECM) using ZView software (Scribner Associates).

When conducting linear EIS, two conditions must be obeyed: (i) the form of the input and output functions must be the same, and (ii) must be linear to ensure that higher harmonic terms are avoided, as these represent irreversible electrochemical changes to the system.[29] In order to ensure these conditions were obeyed, a Kramers-Kronig (K-K) relation was applied to test the linearity, stability and causality of the EIS data. From the impedance spectra, the ionic conductivity,

(K_b) of LiPON was calculated as an input for the electro-chemo-mechanical model using:

$$K_b = \frac{t_{sep}}{A_{sep} R_b} \quad [20]$$

where, $A_{sep}$is the surface area of the SE, and R_b is the bulk resistance of the SE taken from the ECM of the EIS data.

To separate polarisation contributions from the various cell components and identify all time processes in the system, a Fourier transform of the EIS data was performed for distribution of relaxation times (DRT) analysis by,[24,30]

$$Z(w) = R_{ohmic} + Z_{pol}(w) = R_{ohmic} + \sum_{i=1}^{N} \frac{R_{pol,k}}{1 + j\omega\tau_k} \quad [21]$$

where R_{ohmic} is the Ohmic resistance of the SSB and is independent of frequency, while $Z_{pol}(w)$ accounts for the polarisation resistance, $R_{pol,k}$ and is a function of frequency. This deconvolution is possible since the different cell processes have characteristic frequencies, and therefore time constants, associated with specific processes (Table II). h MATLAB code by Wan et al.[30] was used to perform DRT analysis. The K-K residual plots of EIS data were ±1% (Figs. S1 and S2 in the Supporting Information (SI)).

Pulsed electrochemical tests.—The galvanostatic intermittent titration technique (GITT) was used to analyse the total Li^+ ion diffusion of the full cell at different SoCs. Figure S3 in the SI shows the schematic of a typical GITT pulse procedure, where ΔV_t is the voltage response due to the applied current pulse (calculated after subtracting the initial *IR* drop due to internal cell resistance) and the subsequent voltage relaxation, ΔV_s. This method was used to estimate the cell diffusion coefficient, D_{cell} using the equation:

$$D_{cell} = \frac{4}{\pi\tau_{pulse}} t_{elec}^2 \left(\frac{\Delta V_s}{\Delta V_t}\right)^2 \quad [22]$$

where τ_{pulse} is the time period of the GITT pulse and t_{elec} is the electrode thickness. This equation is valid for $\tau_{pulse} << \frac{t_{elec}^2}{D_{cell}}$.[32] In these experiments, 20 s was used for the pulse duration, followed by a relaxation to OCV. The GITT pulses were carried out at 10% SoC intervals and the diffusion coefficients were calculated at these points.

In this configuration, the different electrode contributions are convoluted. To estimate the individual electrode contributions, the positive and negative electrode contributions were scaled by their respective charge transfer resistances, which were determined using DRT analysis (Eq. 21). These estimates of the diffusion coefficients in each electrode were used as parameters in the model.

Load testing.—Hybrid pulse power characterisation (HPPC) testing was performed to probe the dynamic cell behaviour over usable voltage ranges of the cell. The full HPPC protocol is illustrated in Fig. S4 in the SI and yielded three discharge and charge datasets. These were used to parameterise a first order Thevenin ECM, containing a resistor in series with two parallel resistor/capacitor (*RC*) pairs. Separate sets of parameters were developed for discharge and charge. The equivalent circuit is shown in Fig. S5 in the SI.

Parameter extraction was conducted using a script developed in-house, which uses the MATLAB curve-fitting toolbox to fit the ECMs response (i.e. simulated terminal voltage) to the experimental voltage data through a least-squares optimisation method. The methods for extraction follow well established processes, as set out by Ahmed et al.[33] and Jackey et al.[34,35] ECM parameters vary considerably with cell SoC and therefore 5% SoC windows (i.e., 100%–95%, 95%–90%, etc.) were used to extract unique parameters which describe the cell's behaviour for specific SoC ranges.

The simulated terminal voltage (V_t) at any timestep was described by Eq. 23,

$$V_t = U - R_0 I - \sum_{n}^{i=1} U_i U_{RC}, \quad [23]$$

where U is a function a given SoC, R_0 is the series (Ohmic) resistance due to the bulk solid electrolyte impedance R_{bulk}, U_i is the voltage drop across the ith *RC* pair, n is the total number of *RC* pairs ($n = 2$ for the purposes of the present study where, R_{elec} is the lumped charge transfer resistance of the electrodes and R_{diff} is the diffusion resistance) and I is the magnitude of current flow.

Results and Discussion

Formation cycles.—The voltage profiles of the 5 initial charge cycles at C/5 showed a sharp "knee-point" at ≈3.65 V (Fig. 2a). Using differential capacity analysis (Fig. 2b), this feature was attributed to a characteristic LCO phase transformation observed previously[21] and a broad peak due to *a*-Si lithiation to Li_2Si could also be assigned,[28] consistent with *a*-Si not being fully lithiated to $Li_{15}Si_4$ over the voltage range used here. We observed a decrease in the peak area attributed to the *a*-Si electrode on discharge, likely due to side reactions consuming Li during the alloying reaction with *a*-Si on formation, as has been observed in a previous full cell study.[7] Conversely, the differential capacity analysis for 1C cycling post-cell formation (Fig. 2c) showed the peak areas attributed to LCO and *a*-Si to be near equal between charge and discharge—indicative of stable cycling.

Electrochemical testing.—Experimental tests consisting of OCV and low current (C/30) cycling measurements post-formation were used to determine the SoC-OCV relationship and cell capacity respectively. During the OCV testing, a voltage hysteresis was observed between charge and discharge (Fig. 3a), which is commonly seen for *a*-Si-based half-cells.[36] An increased voltage hysteresis was observed during low current (C/30) cycling (Fig. 3b) compared with OCV and was attributed to the hydrostatic stress caused by diffusion induced strains (Eq. 6) as a result of lithiation and delithiation of the *a*-Si electrode. This was consistent with the expected viscoplastic behavior.

Electrochemical impedance spectroscopy and distribution of relaxation times analysis.—Electrochemical impedance spectroscopy (EIS) showed two semi-circles in the high and mid-to-low frequency regions on a Nyquist plot (a representative plot at 50% SoC is shown in Fig. 4a). There was very little variation in the

Table II. Characteristic time scales in the SSB.

Approximate Time Constant (s)	Cell Process Assignment	Source
2×10^{-6}	LiPON ionic migration	Ref. 31
5×10^{-5}	Li_ySi|LiPON interface	This study
3×10^{-4}	Li_ySi|*a*-Si interface	This study
3×10^{-3}	LiPON|LCO charge transfer	Refs. 24, 31

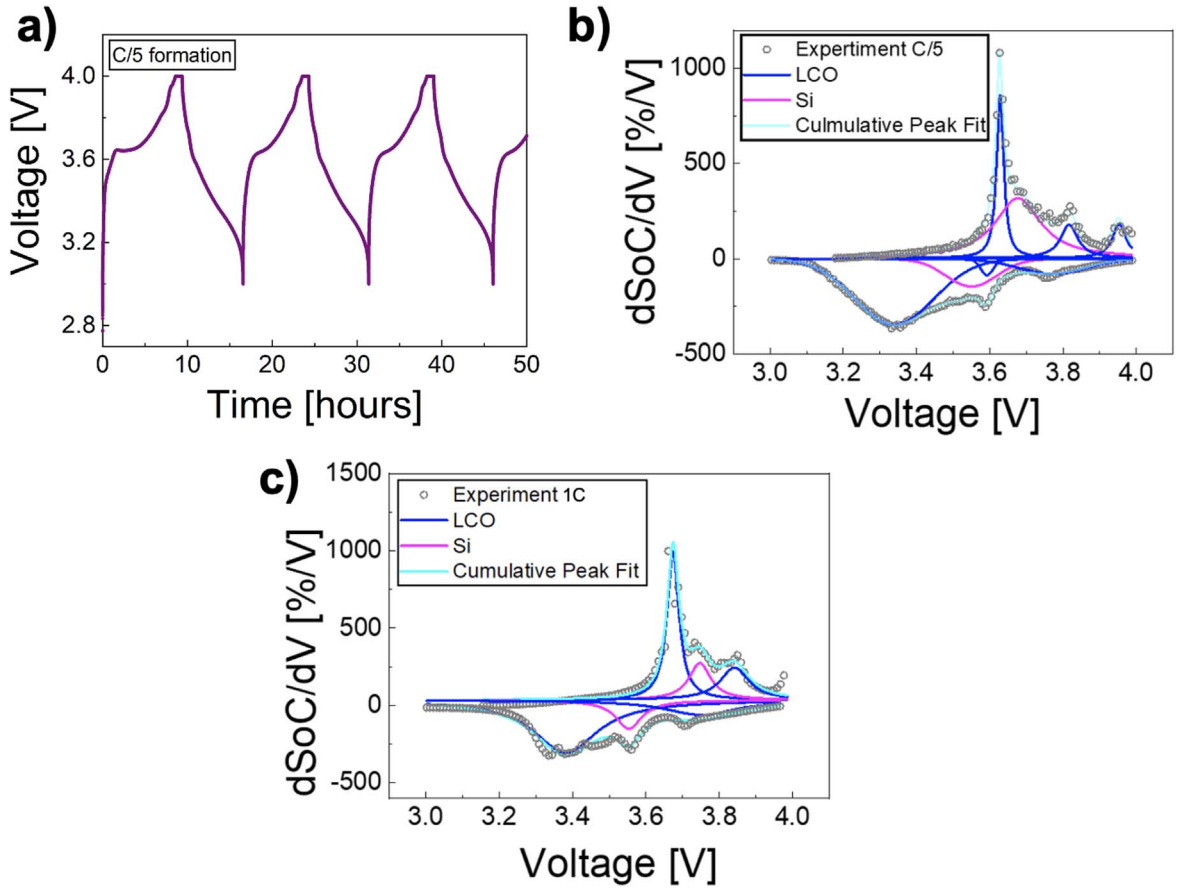

Figure 2. (a) Voltage profiles of C/5 formation cycles. Differential capacity analyses of (b) formation cycle at C/5 and (c) after formation cycles at 1C.

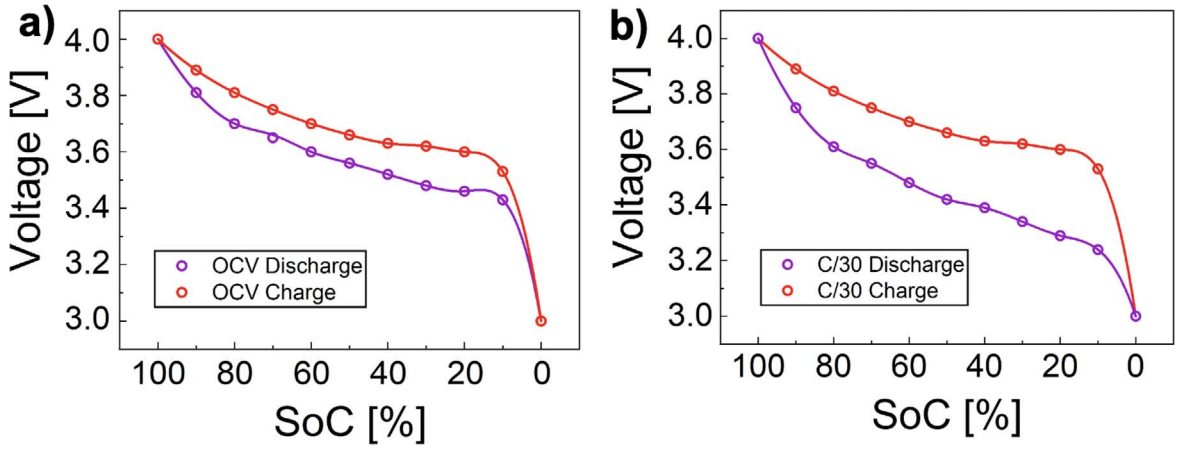

Figure 3. (a) OCV curve on charge and discharge, with 24 h relaxation between SoC points, (b) C/30 cycling. Voltage hysteresis between charge and discharge was observed in both cases.

Nyquist spectra during charge and discharge (Fig. S6 in the SI), thus minimal information could be determined about the internal cell impedances from EIS alone. As the latter semi-circle was substantially depressed, we investigated the possibility that this feature was made up of multiple polarisation processes using DRT analysis.

From the DRT spectrum (Fig. 4b), several distinct polarisation processes were identified. The peak observed at $\approx 10^{-6}$ s was attributed to ion migration in the LiPON SE and was largely invariant during operation as expected. At the other end of the spectrum, the peak at ≈0.1 s was assigned to relatively slow diffusion processes and exhibited a complex dependance with SoC. As low frequency EIS measurements can be unreliable, time-domain experiments were used to deconvolute and quantify individual electrode contributions to the diffusion polarisation in these cells (galvanostatic intermittent titration technique section).

Intermediate polarisation processes in the range 10^{-5} to 10^{-2} s were attributed to charge transfer contributions at the various cell interfaces. Based on previous reports, a single LiPON|LCO time constant was expected to occur at $\approx 10^{-3}$ s (Table II),[24,31] thus, the peaks at $\approx 10^{-5}$ and $\approx 10^{-4}$ s were attributable to the *a*-Si electrode. The exact meaning of these processes is not known, but we speculate they may result from the Li_ySi alloy at the SE| *a*-Si interface and the additional interface between lithiated Li_ySi and unlithiated *a*-Si in the electrode bulk. This picture is consistent with partial *a*-Si

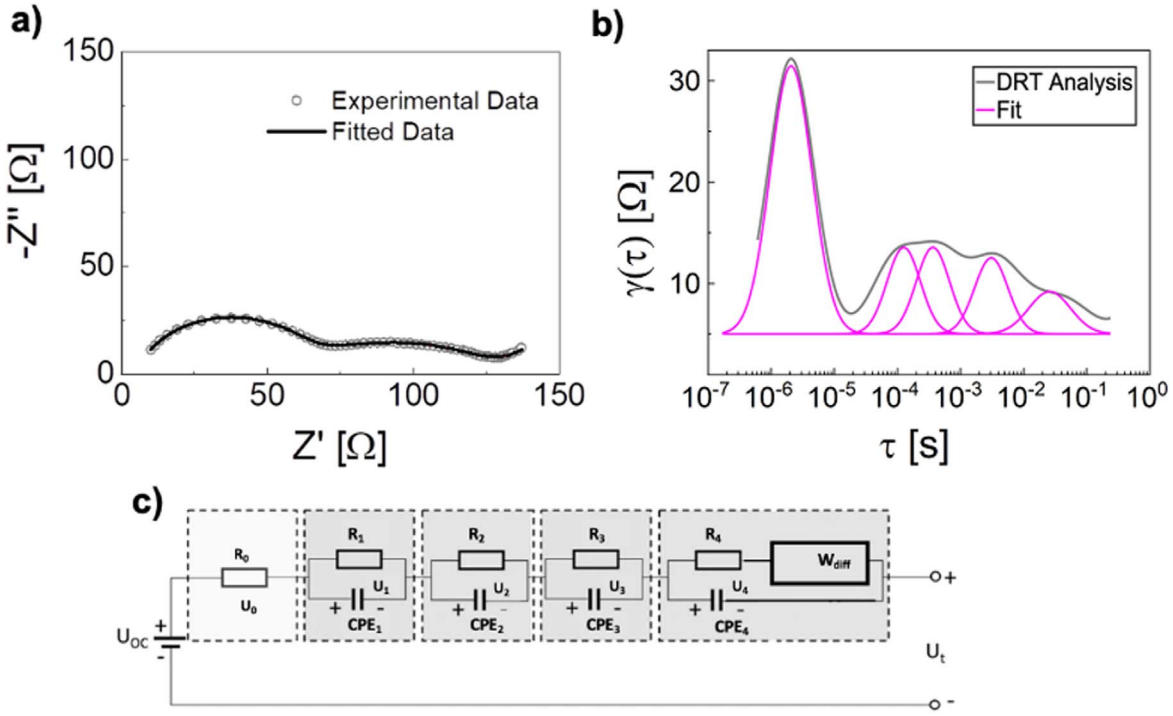

Figure 4. For the discharge case at 50% SoC, (a) representative EIS, note that the axes are non-symmetrical for clarity, (b) deconvoluted DRT spectra showing five polarisation processes and (c) the ECM used for the EIS fitting.

lithiation during operation and the differential capacity analysis which hinted at irreversible Li loss after the first formation cycle (formation cycle section).

During charge and discharge, the SE|LCO polarisation was approximately constant, as was the *a*-Si electrode process centred around $\approx 10^{-5}$ s (Fig. 5). In contrast, the *a*-Si contribution at $\approx 10^{-4}$ s was invariant on delithiation but increased during lithiation. The observed increase in charge transfer resistance may be due to the swelling of *a*-Si as it lithiates to Li_ySi. Therefore, we make the following preliminary assignments: the faster interfacial process ($\approx 10^{-5}$ s) represents the SE|Li_ySi interface, while slower charge transfer ($\approx 10^{-4}$ s) occurs between Li_ySi and bulk *a*-Si.

The five polarisation processes revealed by DRT analysis were incorporated into an ECM that fit the EIS data well as shown in Fig. 4c. The ionic conductivity of LiPON was calculated using the value of R_1 obtained from the ECM fit and inputted into Eq. 20, which was in good agreement with literature values.[24] DRT analysis also allowed quantification of the electrode resistances during charge and discharge, which were used to estimate Li diffusion coefficients for individual electrodes from full-cell galvanostatic intermittent titration technique data in the following section.

Galvanostatic intermittent titration technique.—From experiments using the galvanostatic intermittent titration technique (GITT) the total cell diffusion was extracted. The Li diffusion coefficients, D_{GITT} in the *a*-Si and LCO electrodes were estimated for charge and discharge as explained in pulsed electrochemical tests section. The D_{GITT} value in *a*-Si was determined to be ≈2 orders of magnitude smaller than the D_{GITT} value in LCO (Fig. 6).

For the charge case at low SoC, D_{GITT} was fairly constant but gradually increased from mid to high SoC. A similar trend was found for diffusion on discharge, though a reduction in D_{GITT} was more pronounced in the low SoC region at the end of discharge. This behaviour could be due to hindered extraction of Li^+ ions from *a*-Li_ySi with low Li content. Similarly, the reduced D_{GITT} value in LCO at low SoC on discharge relative to charge can be explained by the intercalation of Li^+ ions into LCO being impeded by a high Li concentration at the LCO|SE interface.

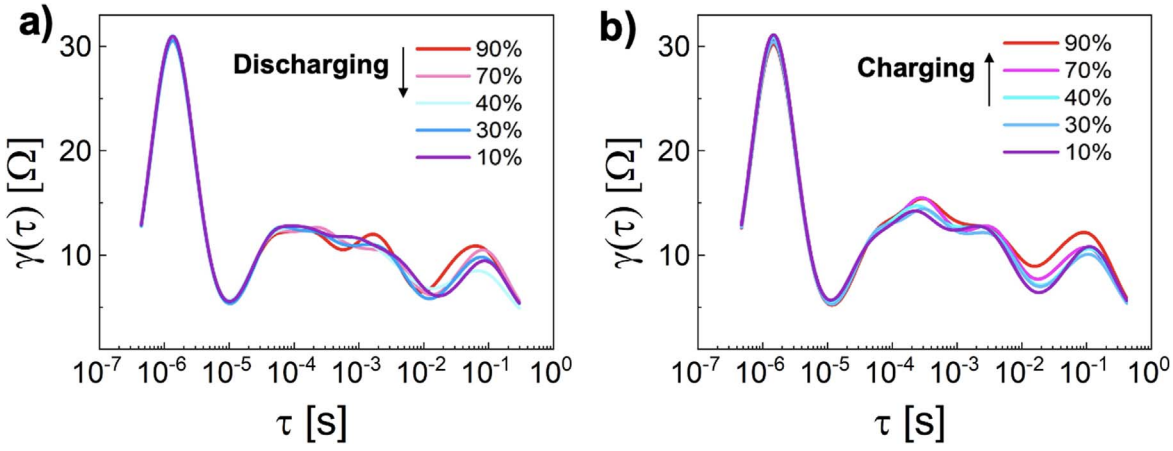

Figure 5. DRT spectra during (a) discharge and (b) charge for various SoC values.

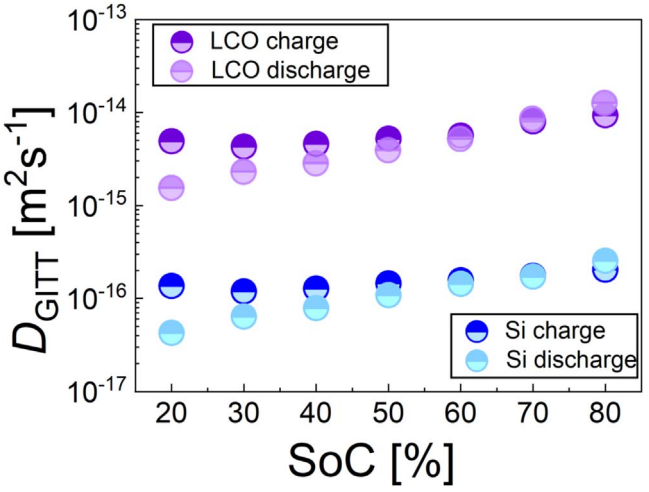

Figure 6. Solid-state diffusion coefficient values estimated for LCO and *a*-Si during charge and discharge using the relative polarisation contributions from DRT analyses.

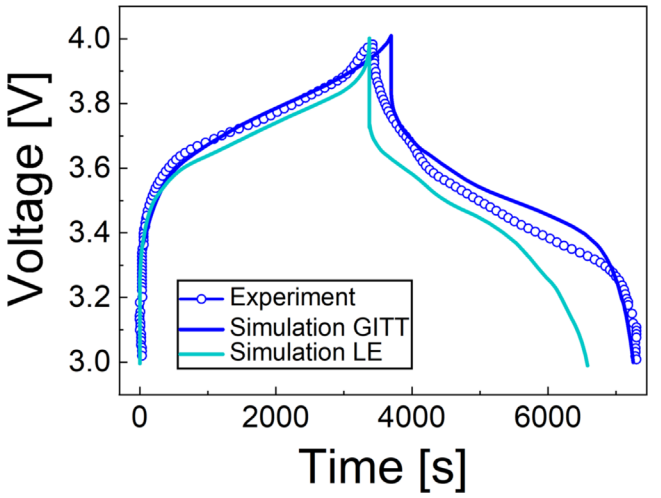

Figure 8. 1C charge/discharge data compared with simulations using experimentally determined diffusion coefficients using GITT vs values from half-cells with a liquid electrolyte (LE).

Hybrid pulse power characterisation.—Hybrid pulse power characterisation (HPPC) was conducted, and the resultant voltage profile was fit to two parallel *RC* units in series. The following *R* values were extracted as a function of SoC: R_{bulk}, R_{elec} and R_{diff}. Figures 7a and 7b shows their behaviour during charge and discharge respectively. The charge profile was diffusion-limited especially at high SoC and the resistance associated with the SE, R_{bulk}, remained approximately constant over the SoC range whereas the charge transfer resistance, R_{elec} had a complex dependence on SoC. However, during discharge there was high diffusion resistance at the SoC extremes but was overall limited by the slow electrode kinetics (higher R_{elec}) with R_{bulk} remaining approximately constant over the SoC range. This observation is in contrast with the EIS results at steady state which showed the charge transfer resistances to be near equal at different SoC points (Fig. 5). If the increase in interfacial resistance R_{elec} was due to irreversible side reactions or a stable decomposition layer, then this should have been apparent in the EIS data (which were measured after HPPC pulsing). Rather, these results suggest that the increase in diffusion impedance, R_{diff} during pulsing was a transient cell response that was due to diffusion limitation in the electrodes (increase in R_{diff}) and mechanical stress due to the build-up of concentration gradients at the SE|electrode interface (increase in R_{elec}).

While diffusion limitations at low SoC during discharge were in agreement with the GITT results, those observed during charging at high SoC were not. Thus, the dynamic cell behaviour is highly complex, especially in the case of charging when *a*-Si strain is increasing. It is possible that the time constants of charge transfer and diffusion processes overlap and therefore R_{elec} and R_{diff} cannot be solely attributed to one or the other, rather one may dominate in certain time domains. Two additional HPPC measurements for charge and discharge were conducted and used for model parameterisation and validation against the experimental data as shown in Figs. S7 and S8 in the SI. These followed similar trends, which was expected for pulses at similar C-rates. An acceptable root mean square (rms) error of $<$15 mV (predicted by the Thevenin model in Figs. S9–S10 in the SI) was obtained.

Model validation.—The electro-chemo-mechanical model was validated using experimental charge and discharge curves, both taken at a 1C rate. Figure 8 shows a comparison between these experimental data and two simulation cases using different values of the Li^+ ion diffusion coefficient, *D* for the electrode materials, as elaborated below.

In the first case (Fig. 8, light blue trace), the *D* values for LCO and *a*-Si used in the model were based on half-cell experiments using liquid electrolyte reference data (supplied by the SSB manufacturer, Ilika). Although good agreement between experiment and simulation was observed on charge, significant deviations ($>$200 mV) were apparent on discharge and the discharge capacity was severely underpredicted. In the second case (Fig. 8, dark blue trace), D_{GITT} values for LCO and *a*-Si were estimated using our full-cell

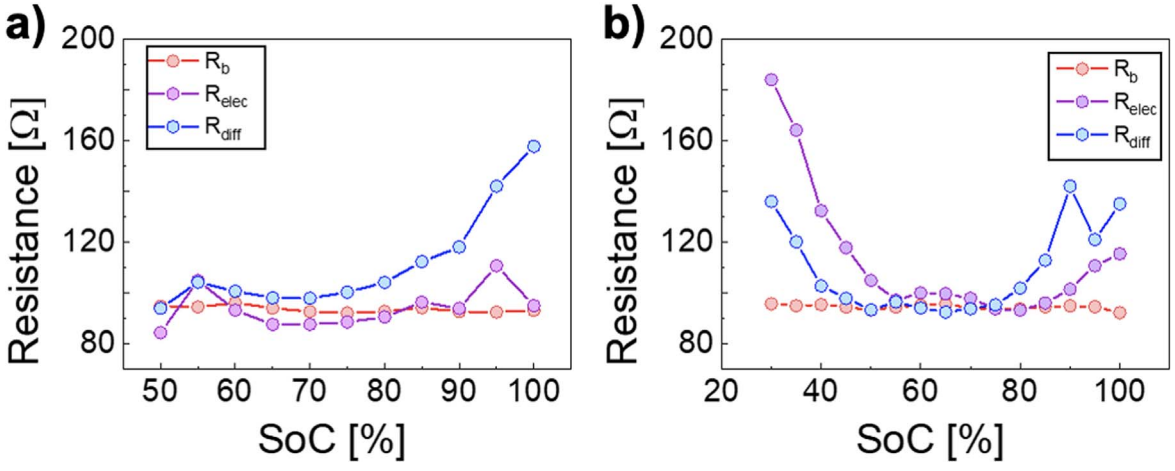

Figure 7. Resistance values extracted from hybrid pulse power characterisation profiles during (a) charge and (b) discharge.

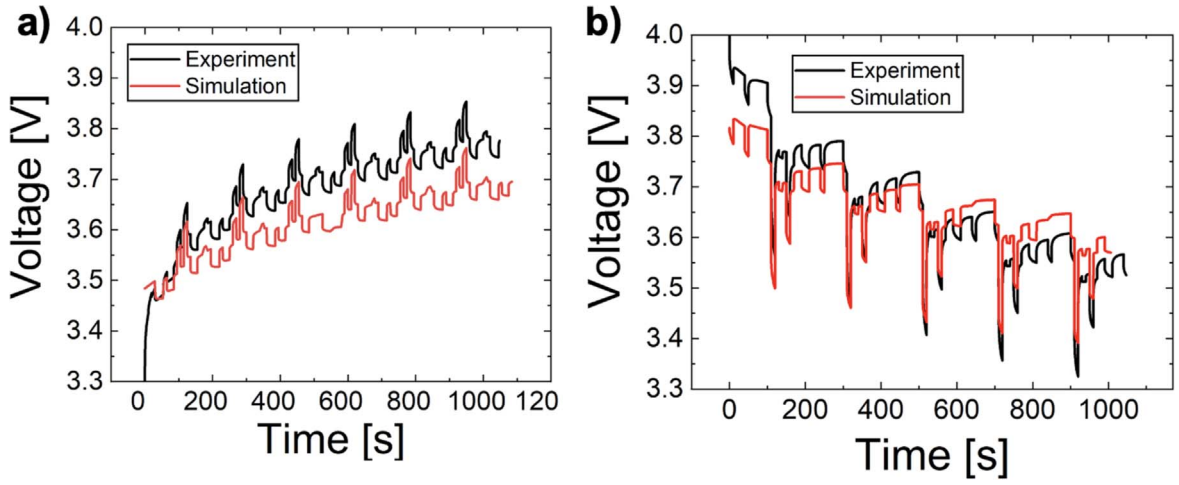

Figure 9. Experimental and simulated HPPC profiles for (a) charge and (b) discharge.

GITT data (GITT section), modified by the total electrode charge transfer resistances (quantified by DRT analysis). The inclusion of these parameters markedly improved the agreement with experiment on discharge, accurately predicting cell capacity and highlighting the importance of accurate diffusion coefficient values when modelling these systems.

The remaining discrepancies between model and experiment during cycling were primarily attributed to uncertainties in the OCV values of *a*-Si and LCO, which were extracted from half-cell data using a liquid electrolyte. When a liquid electrolyte is used, the electrodes can expand freely with minimal constraint. In contrast, the SSB considered in the present study uses a SE that may influence electrode response, e.g. volumetric expansion may be limited by the high Young's modulus of the SE. Given that there will be a change in the stress and strain fields, the OCV is likely to be affected. Representative solid-state half-cell data are therefore highly desirable for future SSB modelling studies.

The model was further validated against charge and discharge during HPPC (Fig. 9). The HPPC simulations followed the profile and general trend of the experimental data well, deviating by a maximum value of ≈100 mV. These offsets can be explained by considering the simulated 1C charge data in Fig. 8, which did not perfectly capture the "knee point" at high SoC. We speculate that this difference has also translated into the HPPC charge profile as a voltage offset. During discharge, the initial pulse was captured as a sharper drop in voltage than observed experimentally, again consistent with the 1C discharge data (Fig. 8). It can be concluded that the model reproduced the pulse behaviour of the cell with further improvement being possible with more accurate experimental parameters extracted from representative half-cell OCV and GITT data.

Electrode thickness effects.—Increasing electrode thickness is desirable to maximise cell capacity but may compromise power capability. In order to aid SSB design, we studied the effects of electrode thickness on stresses and strains in *a*-Si -based, thin-film SSBs. Maps of maximum principal nominal strains and stresses (which both occurred at the SE|Li_ySi interface during 1C cycling) as a function of relative electrode thickness were created using the developed model.

Figure 10 illustrates the tradeoff that exists in terms of limiting the maximum stress and volumetric expansion. As the electrode thickness ratio (nominally a negative to positive electrode thickess ratio of 1:1) was increased to 4:1, the model predicted a maximum strain of −13% and a maximum stress of +30%. By targeting a thicker *a*-Si electrode, which can incorporate more Li, the strain is reduced provided the LCO electrode remains relatively thin, i.e. the degree of *a*-Si lithiation remains relatively low. However, this direction may not be practical from an application perspective, as the cell capacity is limited by the LCO and scales linearly as a function of LCO thickness. For thicker LCO layers, the increase in the total Li available results in a greater degree of lithiation in the *a*-Si, and hence greater strain. Tailoring the relative electrode thicknesses compared to the nominal 1:1 up to a factor of 1:4 (negative to positive electrode thickess ratio), resulted in increased stress from 0.71 GPa up to 1.17 GPa, corresponding to a volumetric

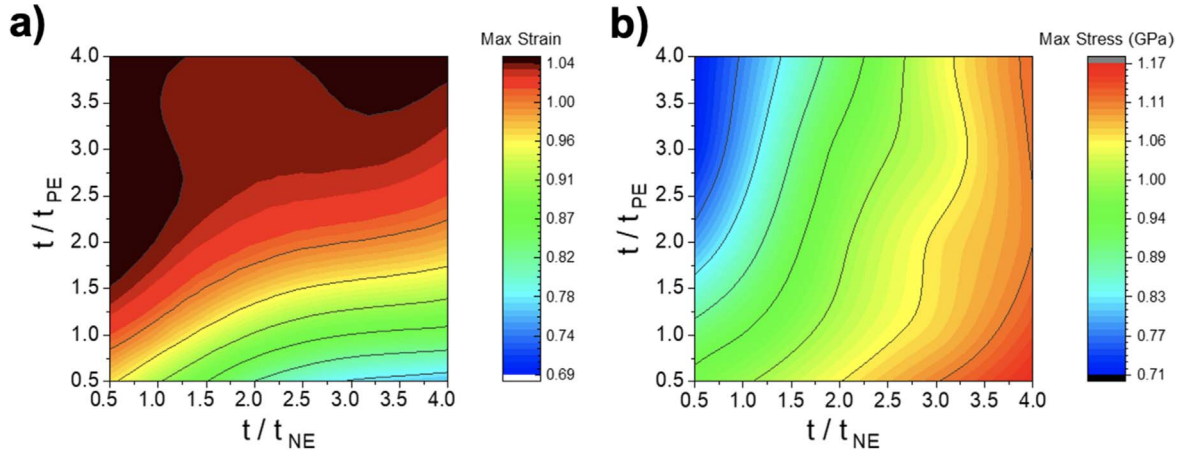

Figure 10. Maps of SSB (a) strain and (b) stress as a function of varying positive and negative electrode thicknesses against the nominal thickness *t*, t/t_{NE} and t/t_{PE} respectively.

expansion from 69% to 104%. Our model showed that stress and strain variations are heterogenous in the cell, with the SE|Li_ySi interface experiencing the greatest stress. Thus, a thin *a*-Si electrode coupled with a thick LCO electrode would be desirable to minimise overall stress. Although this results in a highly lithiated and highly strained *a*-Si electrode, a lower concentration gradient was produced resulting in more a homogenous stress distribution while maximising cell capacity.

We note that our model used an unconstrained *a*-Si electrode for simplicity. In practice this will not be the case, as the top CC and casing will constrain expansion to some extent. As the maximum stress is experienced at the SE|Li_ySi interface, it is critical that the SE mechanical properties are tailored to reduce the *a*-Si stress and be sufficiently mechanically strong to withstand the stresses occurring during cycling, otherwise fracture propagation may occur and cause cell failure. Future work will investigate the relationship between external pressure and stress-strain to inform cell design as well as the mechanical properties of suitable SE candidates for *a*-Si SSBs.

Conclusions

This study has presented experimental characterisation of a commercial thin-film SSB which was used to parameterise and validate a 2D electro-chemo-mechanical model. First, differential capacity analysis during first cycle formation was suggestive of a thin Li_ySi layer forming at the *a*-Si|LiPON interface. The voltage hysteresis observed during OCV and C/30 cycling was attributed to due to diffusion induced stress, highlighting the role of mechanical properties in this system even at low C-rates. DRT analysis was used to guide the interpretation of EIS, which displayed 5 different time processes occurring within the SSB. Two polarisation processes were assigned to the *a*-Si electrode, possibly due to a Li_ySi alloy layer at the *a*-Si|SE interface and an additional interface between this layer and unlithiated *a*-Si in the electrode bulk. This picture is consistent with partial *a*-Si lithiation during operation and irreversible Li loss after the first formation cycle. The diffusion coefficients of *a*-Si and LCO were estimated using the GITT and the pulsed behaviour of the SSB probed using HPPC. HPPC revealed the complex behaviour of the diffusion and electrode resistances as a function of SoC which was not observed during steady-state EIS measurements.

Several experimental parameters extracted from these tests were inputted into the model for validation. It was found that the use of solid-state diffusion coefficient values from half cells using a liquid electrolyte resulted in unsatisfactory agreement with charge/discharge data, while those determined using the GITT on the full cell SSB reproduced the cell capacity during 1C cycling and response during HPPC. The simulation could be further improved by obtaining more accurate experimental parameters for the diffusion coefficient and OCV values. Additionally, electro-mechanical studies of solid-state half-cells (*a*-Si|LiPON|Li metal), e.g. using curvature measurements as have been performed on *a*-Si half cells with liquid electrolytes[15,16] would be beneficial for future modelling efforts.

Finally, the model was used to investigate the stress-strain behaviour when electrode thicknesses were varied. A trade-off between limiting the maximum stress and limiting cell expansion was shown. The recommendation from this study is to initially satisfy the required cell capacity by the LCO thickness, followed by using the thinnest *a*-Si layer possible to accommodate Li. This would minimise the stress at the SE|Li_ySi interface and hence the possibility of fracture and delamination. Whilst this would result in increased the interfacial strain, this may be mitigated by engineering the Li_ySi|SE interface or applying external pressure. Future work will thus focus on the relationship between applied pressure and strain and the mechanical properties of suitable SE candidates that enable a reduction in strain at the Li_ySi|SE interface.

Acknowledgments

We thank Ilika Technologies Ltd for providing us with cells and helpful discussions, in particular to Dr Chris Vian. We also thank Dr Ruben Tomlin for his work developing a MATLAB tool to fit the equivalent circuit model parameters in the presented stud We gratefully acknowledge an EPSRC DTP Studentship (EP/R513143/1) and the Faraday Institution [EP/S003053/1, grant numbers: FIRG015, FIRG0026] for funding and UCL for start-up funds. PRS acknowledges the support of The Royal Academy of Engineering (CIET1718/59)

Author Contribution Statement

Pooja Vadhva: formal analysis, conducting experimental research and investigation, model building, visualization, writing—original draft. **Adam Boyce:** formal analysis, model building, research and investigation, writing—model equations implementation. **Alastair Hales:** analysis of HPPC data using MATLAB script and reviewing**. Mei-Chin Pang:** conceptualization and reviewing. **Anisha Patel:** conceptualization, investigation by developing experimental design, research and set-up, review and editing. **Paul Shearing:** funding acquisition, investigation and reviewing. **Gregory Offer:** conceptualization, review and editing, investigation and visualization. **Alexander Rettie:** conceptualization, review and editing, funding acquisition, investigation and visualization.

ORCID

Pooja Vadhva https://orcid.org/0000-0002-8269-4995
Adam M. Boyce https://orcid.org/0000-0002-8164-1808
Alastair Hales https://orcid.org/0000-0001-6126-6986
Mei-Chin Pang https://orcid.org/0000-0002-6138-3530
Anisha N. Patel https://orcid.org/0000-0002-4914-5062
Paul R. Shearing https://orcid.org/0000-0002-1387-9531
Gregory Offer https://orcid.org/0000-0003-0965-8952
Alexander J. E. Rettie https://orcid.org/0000-0002-2482-9732

References

1. The worldwide micro battery industry is expected to reach $842 Million by 2026 at a CAGR of 20.9% from 2021 - ResearchAndMarkets.comBusiness Wire (https://businesswire.com/news/home/20210723005387/en/The-Worldwide-Micro-Battery-Industry-is-Expected-to-Reach-842-Million-by-2026-at-a-CAGR-of-20.9-from-2021—ResearchAndMarkets.com) (accessed 2021-11-18)T.
2. H. Ning, J. H. Pikul, R. Zhang, X. Li, S. Xu, J. Wang, J. A. Rogers, W. P. King, P. V. Braun, and Global Micro Battery Market, (2021 to 2026), (https://www.prnewswire.com/news-releases/global-micro-battery-market-2021-to-2026—integration-of-micro-batteries-in-smart-textiles-presents-opportunities-301340233.html (accessed 2021–11–18). https://doi.org/10.1073/PNAS.1423889112/-/DCSUPPLEMENTAL)" Integration of micro batteries in smart textiles presents opportunities." *Proceedings of the National Academy of Sciences of the United States of America*.
3. H. J. Bang, S. Kim, and J. Prakash, "Electrochemical investigations of lithium-aluminum alloy anode in li/polymer cells." *J. Power Sources*, **92**, 45 (2001).
4. R. Miyazaki, N. Ohta, T. Ohnishi, I. Sakaguchi, and K. Takada, "An amorphous Si film anode for all-solid-state lithium batteries." *J. Power Sources*, **272**, 541 (2014).
5. D. H. S. Tan et al., "Carbon free high loading silicon anodes enabled by sulfide solid electrolytes for robust all solid-state batteries." *Science*, **373**, 1494-1499 (2021).
6. W. Ping, C. Yang, Y. Bao, C. Wang, H. Xie, E. Hitz, J. Cheng, T. Li, and L. Hu, "A Silicon anode for garnet-based all-solid-state batteries: interfaces and nanomechanics." *Energy Storage Mater.*, **21**, 246 (2019).
7. C. Chen, J. F. M. Oudenhoven, D. L. Danilov, E. Vezhlev, L. Gao, N. Li, F. M. Mulder, R.-A. Eichel, and P. H. L. Notten, "Origin of degradation in Si-based all-solid-state li-ion microbatteries." *Adv. Energy Mater.*, **8**, 1801430 (2018).
8. H. Fathiannasab, L. Zhu, and Z. Chen, "Chemo-mechanical modeling of stress evolution in all-solid-state lithium-ion batteries using synchrotron transmission X-ray microscopy tomography." *J. Power Sources*, **483**, 229028 (2021).
9. H. Sitinamaluwa, J. Nerkar, M. Wang, S. Zhang, and C. Yan, "Deformation and failure mechanisms of electrochemically lithiated silicon thin films." *RSC Adv.*, **7**, 13487 (2017).
10. E. G. Herbert, N. J. Dudney, M. Rochow, V. Thole, and S. A. Hackney, "On the mechanisms of stress relaxation and intensification at the lithium/solid-state electrolyte interface." *J. Mater. Res.*, **34**, 3593 (2019).

11. S. Cangaz, F. Hippauf, F. S. Reuter, S. Doerfler, T. Abendroth, H. Althues, and S. Kaskel, "Enabling high-energy solid-state batteries with stable anode interphase by the use of columnar silicon anodes." *Adv. Energy Mater.*, **10**, 2001320 (2020).
12. Y. Tian, Y. An, C. Wei, H. Jiang, S. Xiong, J. Feng, and Y. Qian, "Recently advances and perspectives of anode-free rechargeable batteries." *Nano Energy.*, **1**, 105344 (2020).
13. L. Baggetto, R. A. H. Niessen, F. Roozehoom, and P. H. L. Notten, "High energy density all-solid-state batteries: a challenging concept towards 3D integration." *Adv. Funct. Mater.*, **18**, 1057 (2008).
14. Z. Xie, Z. Ma, Y. Wang, Y. Zhou, C. Lu, M. Pharr, Z. Suo, and J. J. Vlassak, "Variation of stress with charging rate due to strain-rate sensitivity of silicon electrodes of li-ion batteries." *RSC Adv.*, **270**, 569 (2016).
15. G. Bucci, S. P. V. Nadimpalli, V. A. Sethuraman, A. F. Bower, and P. R. Guduru, "Measurement and modeling of the mechanical and electrochemical response of amorphous si thin film electrodes during cyclic lithiation." *J. Mech. Phys. Solids*, **62**, 276 (2014).
16. C. V. Di Leo, E. Rejovitzky, and L. Anand, "Diffusion–deformation theory for amorphous silicon anodes: the role of plastic deformation on electrochemical performance." *Int. J. Solids Struct.*, **67–68**, 283 (2015).
17. M. Pharr, Z. Suo, and J. J. Vlassak, "Variation of stress with charging rate due to strain-rate sensitivity of silicon electrodes of li-ion batteries." *J. Power Sources*, **270**, 569 (2014).
18. M. Wang and M. Wang, "Simulation of amorphous silicon anode in lithium-ion batteries." *Simulation of amorphous silicon anode in lithium-ion batteries*, Michigan State University (2017), p. 144.
19. K. E. Thomas-Alyea and T.-A. Newman, *J. Electrochemical Systems* (Wiley, New York, NY) 3rd; ed. (2004).
20. V. A. Sethuraman, V. Srinivasan, A. F. Bower, and P. R. Guduru, "In Situ measurements of stress-potential coupling in lithiated silicon." *J. Electrochem. Soc.*, **157**, A1253 (2010).
21. X.-Y. Qiu, Q.-C. Zhuang, Q.-Q. Zhang, R. Cao, P.-Z. Ying, Y.-H. Qiang, and S.-G. Sun, "Electrochemical and electronic properties of $LiCoO_2$ cathode investigated by galvanostatic cycling and EIS." *Phys. Chem. Chem. Phys.*, **14**, 2617 (2012).
22. R. Xu, Y. Yang, F. Yin, P. Liu, P. Cloetens, Y. Liu, F. Lin, and K. Zhao, "Heterogeneous Damage in Li-Ion batteries: experimental analysis and theoretical modeling." *J. Mech. Phys. Solids*, **129**, 160 (2019).
23. L. H. J. Raijmakers, D. L. Danilov, R. A. Eichel, and P. H. L. Notten, "An advanced all-solid-state li-ion battery model." *Electrochim. Acta*, **330**, 135147 (2020).
24. M.-C. Pang, Y. Hao, M. Marinescu, H. Wang, M. Chen, and G. J. Offer, "Experimental and numerical analysis to identify the performance limiting mechanisms in solid-state lithium cells under pulse operating conditions." *Phys. Chem. Chem. Phys.* (2019).
25. R. Chandrasekaran, A. Magasinski, G. Yushin, and T. F. Fuller, "Analysis of lithium insertion/deinsertion in a silicon electrode particle at room temperature." *J. Electrochem. Soc.*, **157**, A1139 (2010).
26. E. G. Herbert, W. E. Tenhaeff, N. J. Dudney, and G. M. Pharr, "Mechanical characterization of LiPON films using nanoindentation." *Thin Solid Films*, **520**, 413 (2011).
27. R. Koerver, W. Zhang, L. Biasi, S. de; Schweidler, A. O. Kondrakov, S. Kolling, T. Brezesinski, P. Hartmann, W. G. Zeier, and J. Janek, "Chemo-mechanical expansion of lithium electrode materials—on the route to mechanically optimized all-solid-state batteries." *Energy Environ. Sci.*, **11**, 2142 (2018).
28. M. J. Loveridge, M. J. Lain, I. D. Johnson, A. Roberts, S. D. Beattie, R. Dashwood, J. A. Darr, and R. Bhagat, "Towards high capacity li-ion batteries based on silicon-graphene composite anodes and Sub-micron V-doped $LiFePO_4$ cathodes." *Sci. Rep.* (2016)**6**, 1.
29. P. Vadhva, J. Hu, M. J. Johnson, R. Stocker, M. Braglia, D. J. L. Brett, and A. J. E. Rettie, "Electrochemical impedance spectroscopy for all-solid-state batteries: theory, methods and future outlook." *Chem. Electro. Chem*, **8**, 1930 (2021).
30. T. H. Wan, M. Saccoccio, C. Chen, and F. Ciucci, "Influence of the discretization methods on the distribution of relaxation times deconvolution: implementing radial basis functions with DRTtools." *Electrochim. Acta*, **184**, 483 (2015).
31. Y. Iriyama, T. Kako, C. Yada, T. Abe, and Z. Ogumi, "Charge transfer reaction at the lithium phosphorus oxynitride glass electrolyte/lithium cobalt oxide thin film interface." *Solid State Ionics*, **176**, 2371 (2005).
32. R. A. Huggins, "Simple method to determine electronic conductivity and ionic components of the conductors in mixed a review." *Ionics (Kiel)*, **8**, 300 (2002).
33. R. Ahmed, J. Gazzarri, S. Onori, S. Habibi, R. Jackey, K. Rzemien, J. Tjong, and J. Lesage, "Model-based parameter identification of healthy and aged li-ion batteries for electric vehicle applications." *SAE International Journal of Alternative Powertrains*, **4**, 233 (2015).
34. *Generate Parameter Data for Equivalent Circuit Battery Block - MATLAB & Simulink - MathWorks United Kingdom*. (https://uk.mathworks.com/help/autoblks/ug/generate-parameter-data-for-estimations-circuit-battery-block.html) (accessed 2021-10-05).
35. R. A. Jackey, G. L. Plett, and M. J. Klein, "Parameterization of a battery simulation model using numerical optimization methods." *SAE Technical Papers* (2009).
36. B. Lu, Y. Song, Q. Zhang, J. Pan, Y.-T. Cheng, and J. Zhang, "Voltage hysteresis of lithium ion batteries caused by mechanical stress." *Phys. Chem. Chem. Phys.*, **18**, 4721 (2016).